Commun. Comput. Phys.
doi: 10.4208/cicp.190211.060811s

Vol. **12**, No. 2, pp. 433-461
August 2012

Simulating an Elastic Ring with Bend and Twist by an Adaptive Generalized Immersed Boundary Method

Boyce E. Griffith[1] and Sookkyung Lim[2,*]

[1] *Leon H. Charney Division of Cardiology, Department of Medicine, New York University School of Medicine, 550 First Avenue, New York, New York 10016, USA.*
[2] *Department of Mathematical Sciences, University of Cincinnati, 839 Old Chemistry Building, Cincinnati, Ohio 45221, USA.*

Received 19 February 2011; Accepted (in revised version) 6 August 2011

Available online 20 February 2012

Abstract. Many problems involving the interaction of an elastic structure and a viscous fluid can be solved by the immersed boundary (IB) method. In the IB approach to such problems, the elastic forces generated by the immersed structure are applied to the surrounding fluid, and the motion of the immersed structure is determined by the local motion of the fluid. Recently, the IB method has been extended to treat more general elasticity models that include both positional and rotational degrees of freedom. For such models, force and torque must both be applied to the fluid. The positional degrees of freedom of the immersed structure move according to the local linear velocity of the fluid, whereas the rotational degrees of freedom move according to the local angular velocity. This paper introduces a spatially adaptive, formally second-order accurate version of this generalized immersed boundary method. We use this adaptive scheme to simulate the dynamics of an elastic ring immersed in fluid. To describe the elasticity of the ring, we use an unconstrained version of Kirchhoff rod theory. We demonstrate empirically that our numerical scheme yields essentially second-order convergence rates when applied to such problems. We also study dynamical instabilities of such fluid-structure systems, and we compare numerical results produced by our method to classical analytic results from elastic rod theory.

AMS subject classifications: 65M06, 65M50, 74S20, 76D05

Key words: Immersed boundary method, Kirchhoff rod theory, adaptive mesh refinement.

1 Introduction

In the 1970's, Peskin developed the immersed boundary (IB) method to study the fluid dynamics of heart valves [1, 2]. Since then, the IB method has become widely used for

*Corresponding author. *Email addresses:* boyce.griffith@nyumc.org (B. E. Griffith), limsk@math.uc.edu (S. Lim)

simulating dynamic problems of fluid-structure interaction in which an elastic structure is immersed in a viscous incompressible fluid [3]. The IB method uses Lagrangian variables to describe the motion of the elastic structure and Eulerian variables to describe the motion of the fluid. In the conventional IB formulation of such problems, the elastic structure applies forces to the fluid that generally act to alter the fluid motion, and the structure moves according to the local velocity of the fluid.

More recently, a generalization of the IB method was introduced to study the dynamics of elastic rods that are modeled using a version of Kirchhoff rod theory [4,5]. Kirchhoff rod theory describes the force and torque generated by an elastic rod in terms of the position of its center line together with a Lagrangian field of orthonormal director vectors that are attached to that center line. These director vectors are rotational degrees of freedom that account for the bending and twisting of the rod. Such representations are useful for describing the motion of filamentous structures like DNA and cables [6–8]. To couple such generalized elasticity models to the fluid within the IB framework, it was necessary to extend the IB formulation to treat elastic structures that are represented in terms of both positional and rotational degrees of freedom. The key features of this generalized IB method are that it applies both the force and the torque generated by the elastic rod to the fluid, and that the elastic rod moves according to both the local linear and angular velocities of the surrounding fluid. Specifically, the local linear velocity determines the motion of the center line, and the local angular velocity determines the rotation of the orthonormal triad of director vectors attached to the structure. So far, this generalized IB method has been used exclusively for problems involving the dynamics of elastic rods immersed in fluid; however, this generalized IB framework is not restricted to such structural models, and it may ultimately find use in coupling other elasticity models that include both positional and rotational degrees of freedom, such as elastic shells, to a surrounding fluid.

The original generalized IB method employed a uniform discretization of the equations of motion that was only first-order accurate [4, 5]. In this work, we introduce an adaptive, formally second-order accurate version of the method. Our numerical scheme is based on a discretization approach previously adopted in adaptive versions of the conventional IB method [9–13]. We use a staggered-grid (i.e., maker-and-cell or MAC [14]) version of the IB method, in which the Eulerian fluid pressure is approximated at the centers of the cells of a locally refined Cartesian grid, and in which the normal components of the Eulerian fluid velocity field are approximated at the centers of the faces of the Cartesian grid cells. Our adaptive three-dimensional discretization is therefore similar, but not identical, to the two-dimensional adaptive version of the conventional IB method described by Roma et al. [9], and to the adaptive three-dimensional IB method described by Griffith [13]. As discussed by Griffith [15], staggered-grid IB methods appear to have clear advantages in terms of volume conservation and resolution of pressure discontinuities when compared to collocated IB discretizations, such as those used in earlier cell-centered adaptive IB methods [10–12].

We assess the convergence properties of our adaptive method via an empirical con-

vergence study that indicates that our scheme converges at a second-order rate. Although we employ an adaptive Eulerian discretization that suffers from a localized reduction in accuracy at interfaces in Cartesian grid resolution (i.e., at coarse-fine interfaces), our results suggest that this reduction in accuracy does not dominate the convergence properties of our scheme at grid spacings that are currently practical for three-dimensional simulations. Although the conventional IB method has been empirically demonstrated to converge at a second-order rate for sufficiently smooth problems in two spatial dimensions [10,16,17], we are not aware of similar empirical convergence results in three spatial dimensions for either the conventional or the generalized IB method.

The instability of open elastic rods and closed elastic rings plays an important role in the modeling of supercoiling DNA and nonlinear cable dynamics [6–8, 18–20] and is a topic that is well-suited for study by the generalized IB method. For instance, the twisted but intrinsically straight elastic ring becomes unstable if the twist about the center line of the ring is sufficiently large. Such rings show writhing dynamics and form coiled configurations with multiple loops, including figure-of-eight and three- and four-leaf clover shapes. For smaller twist values, however, the twisted but intrinsically straight elastic ring remains stable. Thus, there exists a critical twist, below which the ring is stable, and above which the ring is unstable. As described by Goriely [21], the study of the instability of twisted rings dates at least to the work of Michell [22], who determined the critical twist in terms of the ratio of torsional to flexural rigidity. Michell analyzed the linearized dynamics of rings and determined the critical value of twist by constructing nontrivial periodic solutions of the linearized static equations. A century later, Goriely derived the same criterion for the critical twist through a perturbation analysis. Michell and Goriely both found that the value of the critical twist depends both on the ratio of the twisting modulus to the bending modulus, and also on the radius of the ring. As the twist of the ring increases, the torsional strain energy of the ring increases, and in unstable cases, the deformations of the ring convert this torsional energy into bending energy. The instability of elastic rings with constant intrinsic curvature has also been studied [21, 23–27]. It has been observed both experimentally and theoretically that the equilibrium configurations of the intrinsically curved ring are different than those of the intrinsically straight ring [23, 28, 29]. In particular, it is expected that there are no stable solutions without self-contact in cases in which the ring is intrinsically curved [23, 27].

In this paper, we use the adaptive generalized IB method to perform a dynamic instability analysis of elastic rings that are immersed in a viscous incompressible fluid. We consider three cases: elastic rings that are intrinsically straight; elastic rings that are intrinsically curved; and elastic rings that possess only local regions of intrinsic curvature. An elastic rod is said to be intrinsically straight or intrinsically curved if the stress-free configuration of the rod is straight or curved, respectively. For intrinsically straight rings, we find that the critical values of the twist density $\tau = \tau_c$ obtained by our computer simulations agree well with values predicted by classical elastic rod theory. We also find that the value of τ_c is insensitive to the effective thickness of the ring. For twist densities τ below the critical value τ_c, the initial circular configuration of the ring is stable, but for

$\tau > \tau_c$, the initial circular configuration of the ring is unstable. In an unstable case, the ring adopts a supercoiling configuration. There are two types of supercoiling configurations: plectonemic configurations and toroidal configurations. Plectonemic configurations have a small number of terminal loops, and part of the ring tightly coils around the other part of the ring. (Typical plectonemic configurations are shown in Fig. 7(a) with $\tau = 1.6$, and in Fig. 7(b) with $\tau = 1.2$.) Toroidal configurations have multiple terminal loops, and the ring coils around a central axis. (Typical toroidal configurations are shown in Fig. 7(a) with $\tau = 2$, and in Fig. 7(b) with $\tau = 1.6$ and 2.) For intrinsically curved rings, we do not find stable circular, plectonemic, or toroidal configurations. Instead, in this case, the initially curved ring forms either a multicovered ring at lower twist densities, or a tangled structure at larger twist densities. Finally, for rings with only localized regions of nonzero intrinsic curvature, we find the existence of noncircular stable configurations without self-contact at zero twist density. For larger twist densities, the locally curved rings deform into either a plectonemic or a toroidal configuration. These findings are all in good agreement with previous experimental, theoretical, and numerical results [4–8, 18–23, 23–29].

2 The continuous equations of motion

We provide only a brief overview of the generalized IB method; see Peskin [3] for further details on the standard IB method, and see Lim et al. [4] and Lim [5] for further details on the present generalization of the IB method. We use an Eulerian description of the fluid, with $\mathbf{x} = (x_1, x_2, x_3) \in U$ denoting Cartesian physical coordinates and with $U \subset \mathbb{R}^3$ denoting the physical region occupied by the fluid. We assume for simplicity that the fluid possesses a constant mass density ρ and dynamic viscosity μ, and that the region U is periodic. To model the elasticity of the rod, we use a version of Kirchhoff rod theory. This permits us to describe the three-dimensional elastic rod as a three-dimensional space curve that is parametrized by a Lagrangian coordinate $s \in \Omega$, with $\Omega \subset \mathbb{R}$ denoting the curvilinear coordinate space, with $\mathbf{X}(s,t) \in U$ denoting the physical position at time t of a material point s attached to the space curve, and with $\left\{\mathbf{D}^1(s,t), \mathbf{D}^2(s,t), \mathbf{D}^3(s,t)\right\}$ denoting the configuration at time t of an orthonormal triad of director vectors attached to material point s. The principal differences between the standard Kirchhoff rod model and the rod model used herein are that, in the standard model, the rod is required to be inextensible and one of the director vectors is constrained to align with $\frac{\partial \mathbf{X}}{\partial s}$, the tangent vector along the center line of the rod. The present rod model instead includes forces that act to keep the rod approximately inextensible and to keep $\mathbf{D}^3$ approximately aligned with $\frac{\partial \mathbf{X}}{\partial s}$. This formulation can therefore be viewed as a penalty method for the standard Kirchhoff rod model. Although the Lagrangian parameter s need not correspond to arc length along the space curve, the forces generated by the model that act to keep the rod approximately inextensible also act to deform the structure so that s corresponds approximately to arc length along the center line of the rod.

The continuous equations of motion of the generalized IB method are [4,5]

$$\rho\left(\frac{\partial \mathbf{u}}{\partial t}(\mathbf{x},t)+\mathbf{u}(\mathbf{x},t)\cdot\nabla\mathbf{u}(\mathbf{x},t)\right)=-\nabla p(\mathbf{x},t)+\mu\nabla^2\mathbf{u}(\mathbf{x},t)+\mathbf{f}(\mathbf{x},t)+\frac{1}{2}\nabla\times\mathbf{n}(\mathbf{x},t), \tag{2.1a}$$

$$\nabla\cdot\mathbf{u}(\mathbf{x},t)=0, \tag{2.1b}$$

$$\mathbf{f}(\mathbf{x},t)=\int_\Omega \mathbf{F}(s,t)\Phi_w(\mathbf{x}-\mathbf{X}(s,t))\,\mathrm{d}s, \tag{2.1c}$$

$$\mathbf{n}(\mathbf{x},t)=\int_\Omega \mathbf{N}(s,t)\Phi_w(\mathbf{x}-\mathbf{X}(s,t))\,\mathrm{d}s, \tag{2.1d}$$

$$\mathbf{U}(s,t)=\int_U \mathbf{u}(\mathbf{x},t)\Phi_w(\mathbf{x}-\mathbf{X}(s,t))\,\mathrm{d}\mathbf{x}, \tag{2.1e}$$

$$\mathbf{W}(s,t)=\frac{1}{2}\int_U (\nabla\times\mathbf{u}(\mathbf{x},t))\,\Phi_w(\mathbf{x}-\mathbf{X}(s,t))\,\mathrm{d}\mathbf{x}, \tag{2.1f}$$

$$\frac{\partial \mathbf{X}}{\partial t}(s,t)=\mathbf{U}(s,t), \tag{2.1g}$$

$$\frac{\partial \mathbf{D}^i}{\partial t}(s,t)=\mathbf{W}(s,t)\times\mathbf{D}^i(s,t), \qquad \text{for } i=1,2,3, \tag{2.1h}$$

in which $\mathbf{u}(\mathbf{x},t)$ is the Eulerian fluid velocity field; $p(\mathbf{x},t)$ is the Eulerian fluid pressure; $\mathbf{f}(\mathbf{x},t)$ and $\mathbf{n}(\mathbf{x},t)$ are the Eulerian elastic force and torque densities (i.e., densities with respect to the physical coordinate system, so that, e.g., $\mathbf{f}(\mathbf{x},t)\,\mathrm{d}\mathbf{x}$ has units of force); $\mathbf{F}(s,t)$ and $\mathbf{N}(s,t)$ are the Lagrangian elastic force and torque densities (i.e., densities with respect to the material coordinate system, so that, e.g., $\mathbf{F}(s,t)\,\mathrm{d}s$ has units of force); $\Phi_w(\mathbf{x})=\Phi_w(x_1)\Phi_w(x_2)\Phi_w(x_3)$ is a smooth, compactly supported kernel function that mediates coupling between Lagrangian and Eulerian variables; and $\mathbf{U}(s,t)$ and $\mathbf{W}(s,t)$ are the linear and angular velocities of the center line of the rod, respectively. Using the same kernel function Φ_w in Eqs. (2.1c)-(2.1f) ensures that energy is conserved during Lagrangian-Eulerian interaction in the continuous equations of motion [4].

The kernel function Φ_w is a smooth function with fixed, finite support. This implies that, generally,

$$\mathbf{U}(s,t)\neq\mathbf{u}(\mathbf{X}(s,t),t) \qquad \text{and} \qquad \mathbf{W}(s,t)\neq\frac{1}{2}(\nabla\times\mathbf{u})(\mathbf{X}(s,t),t), \tag{2.2}$$

i.e., that the linear and angular velocities of material point s of the rod are generally different from the linear and angular velocities of the fluid at position $\mathbf{X}(s,t)$. Instead, the linear and angular velocities of material point s are the local averages of the linear and angular velocities of the fluid in the vicinity of $\mathbf{X}(s,t)$. Although many choices for Φ_w are possible, we set $\Phi_w(r)=\frac{1}{w}\phi\left(\frac{r}{w}\right)$, with

$$\phi(r)=\begin{cases}\dfrac{1}{8}\left(3-2|r|+\sqrt{1+4|r|-4r^2}\right), & 0\le|r|<1,\\ \dfrac{1}{8}\left(5-2|r|-\sqrt{-7+12|r|-4r^2}\right), & 1\le|r|<2,\\ 0, & 2\le|r|.\end{cases} \tag{2.3}$$

This function $\phi(r)$ is the four-point function described by Peskin [3]. It is constructed to satisfy several discrete conditions that are motivated by spatial discretizations of the continuous equations of motion of the standard IB formulation. In the standard IB method, $\phi(r)$ appears only in the discretized equations of motion. In this generalized IB method, however, $\phi(r)$ appears in both the continuous equations and also in the discretization of those equations. Moreover, w is a physical parameter of the continuous equations of motion. This is unlike the standard IB method, in which w is a numerical parameter that is generally set to be proportional to the spatial meshwidth of the Eulerian grid used to discretize the incompressible Navier-Stokes equations. Nonetheless, for the particular form of the function $\Phi_w(\mathbf{x})$ used in this work, it is necessary that w be an integer multiple of the Eulerian meshwidth to ensure that total force and total torque are conserved during Lagrangian-Eulerian interaction. Thus, a particular choice of the physical parameter w constrains the Eulerian discretizations in which force and torque are conserved, and a particular choice of the Eulerian discretization likewise constrains the choices of w.

Because the value of the physical parameter w is proportional to the size of the support of Φ_w, its value can be viewed as controlling the effective thickness of the rod. Specifically, larger (smaller) values of w will yield rods with larger (smaller) effective thicknesses. This notion of the effective thickness of the immersed rod is primarily qualitative, and a precise quantification of the relationship between the value of w and the rod thickness has not yet been established. One approach that could yield such a quantification is an extension of the analysis of Bringley and Peskin [30], who considered the effective size of rigid spheres and slender bodies in the context of the standard IB method in the Stokesian regime.

We now provide an overview of the rod model used in the present work. Let $\mathbf{F}^{\text{rod}}(s,t)$ and $\mathbf{N}^{\text{rod}}(s,t)$ denote the force and moment transmitted across a section of the elastic rod at material point s at time t. The Lagrangian force and torque densities, $\mathbf{F}(s,t)$ and $\mathbf{N}(s,t)$, that are transmitted to the fluid are determined from $\mathbf{F}^{\text{rod}}$ and $\mathbf{N}^{\text{rod}}$ by the equations of linear and angular momentum balance, i.e.,

$$\mathbf{F} = \frac{\partial \mathbf{F}^{\text{rod}}}{\partial s}, \tag{2.4a}$$

$$\mathbf{N} = \frac{\partial \mathbf{N}^{\text{rod}}}{\partial s} + \frac{\partial \mathbf{N}^{\text{rod}}}{\partial s} \times \mathbf{F}^{\text{rod}}, \tag{2.4b}$$

so that

$$\mathbf{f}(\mathbf{x},t) = \int_\Omega \frac{\partial \mathbf{F}^{\text{rod}}}{\partial s}(s,t)\, \Phi_w(\mathbf{x} - \mathbf{X}(s,t))\, \mathrm{d}s, \tag{2.5a}$$

$$\mathbf{n}(\mathbf{x},t) = \int_\Omega \left(\frac{\partial \mathbf{N}^{\text{rod}}}{\partial s}(s,t) + \frac{\partial \mathbf{N}^{\text{rod}}}{\partial s}(s,t) \times \mathbf{F}^{\text{rod}}(s,t) \right) \Phi_w(\mathbf{x} - \mathbf{X}(s,t))\, \mathrm{d}s. \tag{2.5b}$$

$\mathbf{F}^{\text{rod}}$ and $\mathbf{N}^{\text{rod}}$ are determined by the constitutive equations of the special Cosserat theory

of rods [31]. Specifically,

$$\mathbf{F}^{\text{rod}} = F^1\mathbf{D}^1 + F^2\mathbf{D}^2 + F^3\mathbf{D}^3, \tag{2.6a}$$

$$\mathbf{N}^{\text{rod}} = N^1\mathbf{D}^1 + N^2\mathbf{D}^2 + N^3\mathbf{D}^3, \tag{2.6b}$$

$$N^1 = a_1\left(\frac{\partial \mathbf{D}^2}{\partial s}\cdot\mathbf{D}^3 - \kappa_1\right), \tag{2.6c}$$

$$N^2 = a_2\left(\frac{\partial \mathbf{D}^3}{\partial s}\cdot\mathbf{D}^1 - \kappa_2\right), \tag{2.6d}$$

$$N^3 = a_3\left(\frac{\partial \mathbf{D}^1}{\partial s}\cdot\mathbf{D}^2 - \tau\right), \tag{2.6e}$$

$$F^1 = b_1\mathbf{D}^1\cdot\frac{\partial \mathbf{X}}{\partial s}, \tag{2.6f}$$

$$F^2 = b_2\mathbf{D}^2\cdot\frac{\partial \mathbf{X}}{\partial s}, \tag{2.6g}$$

$$F^3 = b_3\left(\mathbf{D}^3\cdot\frac{\partial \mathbf{X}}{\partial s} - 1\right). \tag{2.6h}$$

Here, a_1 and a_2 are the bending moduli of the rod about director vectors $\mathbf{D}^1$ and $\mathbf{D}^2$, respectively, and a_3 is the twisting modulus of the rod about $\mathbf{D}^3$. (Recall that $\mathbf{D}^3$ is approximately aligned with $\frac{\partial \mathbf{X}}{\partial s}$.) In this work, we take $a_1 = a_2 = a$, which corresponds to the case in which the rod has a circular cross section with axially symmetric material properties. The intrinsic curvature of the rod is

$$\kappa = \sqrt{\kappa_1^2 + \kappa_2^2}, \tag{2.7}$$

and the intrinsic twist of the rod is τ. The parameters b_1 and b_2 are shear moduli, and the parameter b_3 is a stretching modulus. In the limit $b_i \to \infty$, $i = 1,2,3$, this model reduces to the standard Kirchhoff rod model, in which the rod is inextensible, s corresponds to arc length along the center line of the rod, and $\mathbf{D}^3 = \frac{\partial \mathbf{X}}{\partial s}$ is the unit tangent vector aligned with the center line of the rod. For finite values of b_i, $i = 1,2,3$, Eqs. (2.6f)-(2.6h) act to keep the rod approximately inextensible, to ensure that s is approximately the arc length along the space curve, and to align $\mathbf{D}^3$ approximately with $\frac{\partial \mathbf{X}}{\partial s}$. For simplicity, we take $b_1 = b_2 = b$, and we also generally set $b_3 = b$.

As has been done previously with the generalized IB method [4], we consider the case in which the elastic rod is a closed ring, and we choose the initial configuration of the ring to be a perturbation of an equilibrium solution of Eqs. (2.4a)-(2.4b) and (2.6a)-(2.6h) in the absence of external loading conditions. This configuration is formulated in terms of cylindrical coordinates (r,θ,z) with unit vectors

$$\mathbf{r}(\theta) = (\cos(\theta), \sin(\theta), 0), \tag{2.8a}$$

$$\boldsymbol{\theta}(\theta) = (-\sin(\theta), \cos(\theta), 0), \tag{2.8b}$$

$$\mathbf{z} = (0,0,1). \tag{2.8c}$$

The initial configuration of the ring is given for $0 \leq s \leq 2\pi r_0$ by

$$\mathbf{X}(s) = r_0 \cos(\beta)\mathbf{r}(s/r_0), \tag{2.9a}$$
$$\mathbf{D}^1(s) = \cos(qs/r_0 + \epsilon\sin(s/r_0))\mathbf{E}(s) + \sin(qs/r_0 + \epsilon\sin(s/r_0))\mathbf{r}(s/r_0), \tag{2.9b}$$
$$\mathbf{D}^2(s) = -\sin(qs/r_0 + \epsilon\sin(s/r_0))\mathbf{E}(s) + \cos(qs/r_0 + \epsilon\sin(s/r_0))\mathbf{r}(s/r_0), \tag{2.9c}$$
$$\mathbf{D}^3(s) = \cos(\beta)\boldsymbol{\theta}(s/r_0) + \sin(\beta)\mathbf{z}, \tag{2.9d}$$

in which r_0 is the radius of the unstressed ring,

$$\mathbf{E}(s) = -\sin(\beta)\boldsymbol{\theta}(s/r_0) + \cos(\beta)\mathbf{z} \tag{2.10}$$

is a reference vector that is orthogonal to $\mathbf{D}^3$ within the plane spanned by $\boldsymbol{\theta}$ and $\mathbf{z}$, and

$$\sin(\beta) = -\frac{a_3 q}{b r_0^2 + a_3 - a}. \tag{2.11}$$

The parameter q is the number of turns along the rod, and ϵ is a perturbation parameter. Note that if q is integer valued, then the orthonormal director vectors are continuous at $s = 0$, which is the periodic image of $s = 2\pi r_0$.

This formulation provides us with two ways of assigning the intrinsic twist of the ring: by setting the value of the parameter q along with $\tau = 0$, or by setting the values of the strain vector $(\kappa_1, \kappa_2, \tau)$ along with $q = 0$. The relation between q and τ is given by

$$\tau = \frac{2\pi q}{c} = \frac{q}{r_0}, \tag{2.12}$$

in which $c = 2\pi r_0$ is the circumference of the unstressed ring. In this work, r_0 is chosen so that $\tau = 0.4q$.

3 Spatial discretization

Our numerical scheme employs a generalization of an adaptive discretization approach used previously with the conventional IB method [9–13]. Specifically, the Eulerian equations are approximated on a three-dimensional block-structured hierarchical Cartesian grid, and the Lagrangian equations are approximated on a moving curvilinear mesh that is aligned with the immersed structure. In this approach, the Lagrangian mesh is not constrained to conform to the configuration of the hierarchical Cartesian grid. Instead, the Eulerian discretization is adaptively updated to conform to the dynamic configuration of the immersed structure. This is done in a manner that ensures that the immersed structure remains embedded within the finest level of the locally refined Cartesian grid.

3.1 Lagrangian discretization

We discretize the Lagrangian equations on a one-dimensional node-centered mesh that is aligned with the center line of the rod. The Lagrangian mesh spacing is taken to be uniform and is denoted by Δs. We use the index l to label the curvilinear mesh nodes, with, e.g., $\mathbf{X}_l$ and $\mathbf{F}_l$ indicating the position and Lagrangian force density associated with node l of the Lagrangian mesh. The nodal values $\mathbf{F}_l$ and $\mathbf{N}_l$ are computed using the nodal values $\mathbf{X}_l$ along with values of $\mathbf{F}^{\text{rod}}$ and $\mathbf{N}^{\text{rod}}$ that are computed at intermediate positions $s_{l+1/2}$. A standard second-order accurate approximation to $\frac{\partial}{\partial s}$ is used to compute the discrete approximations to $\mathbf{F}$, $\mathbf{N}$, $\mathbf{F}^{\text{rod}}$, and $\mathbf{N}^{\text{rod}}$. A slight complication is that the discretization requires approximations to the triad of orthonormal director vectors at intermediate positions $s_{l+1/2}$. These values must be determined in a manner that ensures that the intermediate values $\left\{\mathbf{D}^1_{l+1/2}, \mathbf{D}^2_{l+1/2}, \mathbf{D}^3_{l+1/2}\right\}$ form an orthonormal triad. Complete details of this Lagrangian spatial discretization are presented by Lim et al. [4]. We consider only closed rings in the present work, and therefore we simply impose periodic boundary conditions on the curvilinear mesh.

3.2 Eulerian discretization

We discretize the Eulerian equations on a hierarchical Cartesian grid that is composed of a collection of nested grid levels. The levels of the grid hierarchy are labeled $\ell = 0, \cdots, \ell_{\max}$, with $\ell = 0$ indicating the coarsest level in the hierarchy and with $\ell = \ell_{\max}$ indicating the finest level. Each grid level is composed of one or more rectangular Cartesian grid patches, and all grid patches of a particular grid level ℓ of the hierarchy share the same Cartesian grid spacings, which are denoted Δx^ℓ_1, Δx^ℓ_2, and Δx^ℓ_3. For simplicity, we take $\Delta x^\ell_1 = \Delta x^\ell_2 = \Delta x^\ell_3 = h^\ell$, and we denote by N^ℓ the number of Cartesian grid cells in each coordinate direction that would be required to construct a uniform-grid discretization of level ℓ. With L denoting the length of the computational domain U, we have that $h^\ell = L/N^\ell$. The grid spacings on adjacent levels ℓ and $\ell-1$ of the grid hierarchy are not arbitrary; instead, they are related by an integer refinement ratio $\mathfrak{n}$, so that $h^\ell = h^{\ell-1}/\mathfrak{n}$. Moreover, the faces of the level ℓ grid patches are required to coincide with the faces of the level $\ell-1$ grid cells. The grid levels are constructed to satisfy a proper nesting condition [32], which requires that the physical region covered by the union of the level ℓ grid patches be strictly contained within the region covered by the union of the level $\ell-1$ grid patches. Because it is difficult to visualize such locally refined grids in three spatial dimensions, a representative two-dimensional locally refined Cartesian grid is shown in Fig. 1.

To approximate the incompressible Navier-Stokes equations, we employ an adaptive version of a staggered-grid discretization (i.e., a marker-and-cell or MAC scheme [14]); see Fig. 2. Briefly, the pressure is approximated at the centers of the Cartesian grid cells, and the normal components of the velocity are approximated at the centers of the faces of the Cartesian grid cells. At coarse-fine interfaces in the Cartesian grid, $\mathbf{u}$ is described in terms of the fine-grid values that are defined along such interfaces, not in terms of the

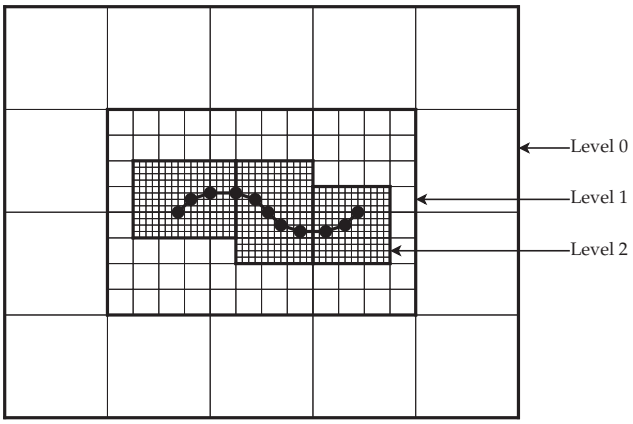

Figure 1: Two-dimensional block-structured hierarchical Cartesian grid consisting of three nested levels, with refinement ratio $\mathfrak{n}=4$ between levels, and with a Lagrangian structure embedded in the finest level of the grid hierarchy. To simplify our scheme, we construct the Cartesian grid hierarchy so that the support of $\Phi_w(\mathbf{x}-\mathbf{X}_l)$ is contained within the finest level of the hierarchy for each Lagrangian mesh node l. This has the effect of ensuring that the immersed structure remains embedded in the finest level of the grid hierarchy throughout the computation.

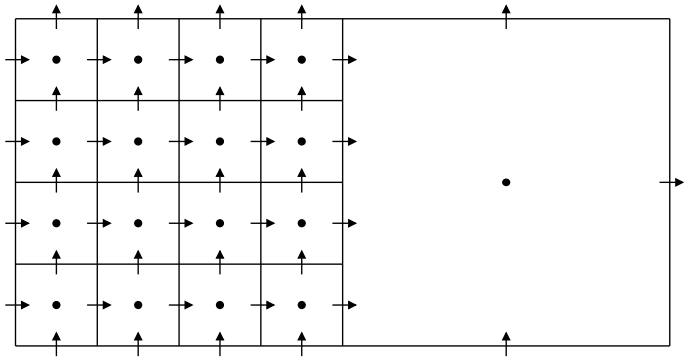

Figure 2: Two-dimensional adaptive staggered-grid (MAC) Eulerian discretization. The fluid pressure p is approximated at the centers of the Cartesian grid cells, and the normal components of the fluid velocity $\mathbf{u}$ are approximated at the centers of the faces of the Cartesian grid cells. At coarse-fine interfaces in the grid hierarchy, $\mathbf{u}$ is described in terms of the fine-grid values that are defined along that interface.

underlying coarse-grid values. We use indices (i,j,k) to label the centers of the Cartesian grid cells and indices $(i-\frac{1}{2},j,k)$, $(i,j-\frac{1}{2},k)$, and $(i,j,k-\frac{1}{2})$ to label the centers of the x_1, x_2, and x_3 faces of the Cartesian grid cells, and we use the notation $p_{i,j,k}$, $(u_1)_{i-\frac{1}{2},j,k}$, $(u_2)_{i,j-\frac{1}{2},k}$, and $(u_3)_{i,j,k-\frac{1}{2}}$ to denote the values of p and $\mathbf{u}$ associated with those locations, respectively.

To construct composite-grid approximations to the Eulerian spatial differential operators of the continuous equations, it is convenient to augment each Cartesian grid patch with a buffer of ghost cells, so that we may use standard uniform-grid finite-difference discretizations of these operators within each patch. Whenever possible, ghost-cell val-

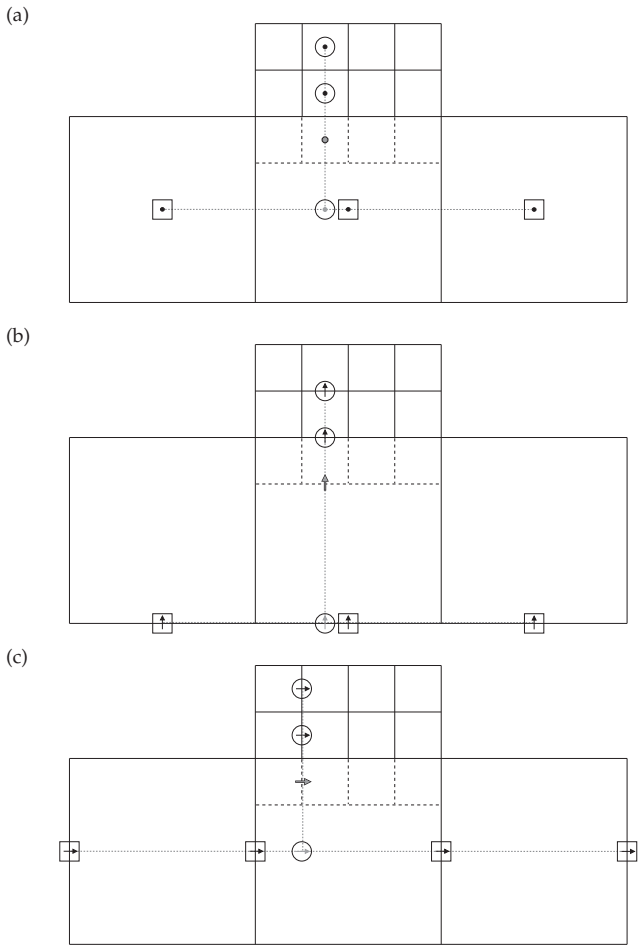

Figure 3: Two-dimensional coarse-fine interface interpolation scheme for (a) cell-centered quantities, (b) face-centered quantities that are normal to the coarse-fine interface, and (c) face-centered quantities that are tangential to the coarse-fine interface. Ghost cells associated with the fine grid patch are indicated by dashed lines. In each case, we first interpolate values in the direction tangential to the coarse-fine interface using either quadratic or cubic interpolation, and then interpolate values in the direction normal to the coarse-fine interface using quadratic interpolation. Values that are interpolated in the initial coarse-grid interpolation are indicated by squares, and values that are interpolated in the final fine-grid interpolation are indicated by circles.

ues associated with a particular level ℓ grid patch are obtained by copying interior values from a neighboring level ℓ grid patch. This is not possible at interfaces in grid resolution, however. Values in ghost cells in the vicinity of such coarse-fine interfaces are obtained by specialized interpolation procedures that use both coarse-grid and fine-grid values. Two-dimensional versions of these coarse-fine interface interpolation procedures are summarized in Fig. 3. These procedures are extensions of the cell-centered coarse-fine interface interpolation approach of Minion [33], Martin and Colella [34], and Martin et al. [35]. Briefly, we first compute an intermediate value by interpolating coarse-grid values in the

directions tangential to the coarse-fine interface using tensor-product interpolation rules based on third- or fourth-order one-dimensional interpolation rules. We then compute the necessary ghost-cell values using quadratic interpolation in the direction normal to the coarse-fine interface. Any coarse-grid value within the interpolation stencil that is covered by fine-grid values is defined in terms of those fine-grid values by tricubic interpolation. These interpolation schemes yield at least third-order accurate interpolants at the ghost cells adjacent to interfaces in grid resolution, so that gradients and curls may be approximated with at least second-order accuracy, and so that the viscous terms may be approximated there with at least local first-order accuracy. See Griffith [13] for further details on this coarse-fine interface interpolation scheme. We emphasize that, away from coarse-fine interfaces, our composite-grid finite-difference discretization is second-order accurate, so that our discretization of the incompressible Navier-Stokes equations is globally second-order accurate.

With the ghost-cell values determined in this manner, we define composite-grid approximations to $\nabla\cdot$, ∇, $\nabla\times$, and ∇^2, as follows. To define $\nabla_h\cdot\mathbf{u}\approx\nabla\cdot\mathbf{u}$, we first ensure mass conservation at coarse-fine interfaces by recursively defining the coarse-grid values of $\mathbf{u}$ to be the averages of any overlying fine-grid values. We then compute at each cell center on level ℓ

$$(\nabla_h\cdot\mathbf{u})_{i,j,k}=\frac{(u_1)_{i+\frac{1}{2},j,k}-(u_1)_{i-\frac{1}{2},j,k}}{h^\ell}+\frac{(u_2)_{i,j+\frac{1}{2},k}-(u_2)_{i,j-\frac{1}{2},k}}{h^\ell}+\frac{(u_3)_{i,j,k+\frac{1}{2}}-(u_3)_{i,j,k-\frac{1}{2}}}{h^\ell}. \tag{3.1}$$

Notice that, unlike the remaining finite-difference approximations, no ghost cell values are required to evaluate $\nabla_h\cdot\mathbf{u}$ within the patch interior. To define $\nabla_h p\approx\nabla p$, we compute at each cell face on level ℓ

$$(\nabla_h p)_{i-\frac{1}{2},j,k}=\frac{p_{i,j,k}-p_{i-1,j,k}}{h^\ell}, \tag{3.2a}$$

$$(\nabla_h p)_{i,j-\frac{1}{2},k}=\frac{p_{i,j,k}-p_{i,j-1,k}}{h^\ell}, \tag{3.2b}$$

$$(\nabla_h p)_{i,j,k-\frac{1}{2}}=\frac{p_{i,j,k}-p_{i,j,k-1}}{h^\ell}. \tag{3.2c}$$

To define $\nabla_h\times\mathbf{u}\approx\nabla\times\mathbf{u}$, we compute at each x_1 cell face on level ℓ

$$\begin{aligned}(\nabla_h\times\mathbf{u})_{i-\frac{1}{2},j,k}=&\frac{1}{8h^\ell}\Big((u_3)_{i-1,j+1,k-\frac{1}{2}}-(u_3)_{i-1,j-1,k-\frac{1}{2}}+(u_3)_{i,j+1,k-\frac{1}{2}}-(u_3)_{i,j-1,k-\frac{1}{2}}\\&+(u_3)_{i-1,j+1,k+\frac{1}{2}}-(u_3)_{i-1,j-1,k+\frac{1}{2}}+(u_3)_{i,j+1,k+\frac{1}{2}}-(u_3)_{i,j-1,k+\frac{1}{2}}\Big)\\&+\frac{1}{8h^\ell}\Big((u_2)_{i-1,j-\frac{1}{2},k+1}-(u_2)_{i-1,j-\frac{1}{2},k-1}+(u_2)_{i,j-\frac{1}{2},k+1}-(u_2)_{i,j-\frac{1}{2},k-1}\\&+(u_2)_{i-1,j+\frac{1}{2},k+1}-(u_2)_{i-1,j+\frac{1}{2},k-1}+(u_2)_{i,j+\frac{1}{2},k+1}-(u_2)_{i,j+\frac{1}{2},k-1}\Big).\end{aligned} \tag{3.3}$$

Similar formulae are used to compute the remaining components of $\nabla_h \times \mathbf{u}$ on the x_2 and x_3 cell faces. To define $\nabla_h^2 \mathbf{u} \approx \nabla^2 \mathbf{u}$, we compute at each x_1 face on level ℓ

$$\begin{aligned}(\nabla_h^2 u_1)_{i-\frac{1}{2},j,k} = & \frac{(u_1)_{i+\frac{1}{2},j,k} - 2(u_1)_{i-\frac{1}{2},j,k} + (u_1)_{i-\frac{3}{2},j,k}}{(h^\ell)^2} \\ & + \frac{(u_1)_{i-\frac{1}{2},j+1,k} - 2(u_1)_{i-\frac{1}{2},j,k} + (u_1)_{i-\frac{1}{2},j-1,k}}{(h^\ell)^2} \\ & + \frac{(u_1)_{i-\frac{1}{2},j,k+1} - 2(u_1)_{i-\frac{1}{2},j,k} + (u_1)_{i-\frac{1}{2},j,k-1}}{(h^\ell)^2}. \end{aligned} \tag{3.4}$$

Similar formulae are used to compute the remaining components of $\nabla_h^2 \mathbf{u}$ on the x_2 and x_3 cell faces. For further details, see Griffith [13].

3.3 Lagrangian-Eulerian interaction

We construct the locally refined Cartesian grid so that the support of $\Phi_w(\mathbf{x} - \mathbf{X}_l)$ is strictly contained within the finest level of grid for each Lagrangian node l; see Section 5 below. This constraint on the configuration of the locally refined grid greatly simplifies our adaptive discretization because it allows us to use approximations to Eqs. (2.1c)-(2.1f), the equations of Lagrangian-Eulerian interaction, that involve only Eulerian values defined on the finest level of the grid.

With $\mathbf{f} = (f_1, f_2, f_3)$ and $\mathbf{F} = (F_1, F_2, F_3)$, we approximate Eq. (2.1c) componentwise by

$$(f_1)_{i-\frac{1}{2},j,k} = \sum_l (F_1)_l \Phi_w(\mathbf{x}_{i-\frac{1}{2},j,k} - \mathbf{X}_l) \Delta s, \tag{3.5a}$$

$$(f_2)_{i,j-\frac{1}{2},k} = \sum_l (F_2)_l \Phi_w(\mathbf{x}_{i,j-\frac{1}{2},k} - \mathbf{X}_l) \Delta s, \tag{3.5b}$$

$$(f_3)_{i,j,k-\frac{1}{2}} = \sum_l (F_3)_l \Phi_w(\mathbf{x}_{i,j,k-\frac{1}{2}} - \mathbf{X}_l) \Delta s, \tag{3.5c}$$

on level $\ell_{\max}$. In regions that are not covered by the finest level of the grid hierarchy, $\mathbf{f}$ is defined to equal zero. Analogous formulae are used to approximate Eq. (2.1d).

With $\mathbf{u} = (u_1, u_2, u_3)$ and $\mathbf{U} = (U_1, U_2, U_3)$, we approximate Eq. (2.1e) componentwise by

$$(U_1)_l = \sum_{i,j,k} (u_1)_{i-\frac{1}{2},j,k} \Phi_w(\mathbf{x}_{i-\frac{1}{2},j,k} - \mathbf{X}_l) \left(h^{\ell_{\max}}\right)^3, \tag{3.6a}$$

$$(U_2)_l = \sum_{i,j,k} (u_2)_{i,j-\frac{1}{2},k} \Phi_w(\mathbf{x}_{i,j-\frac{1}{2},k} - \mathbf{X}_l) \left(h^{\ell_{\max}}\right)^3, \tag{3.6b}$$

$$(U_3)_l = \sum_{i,j,k} (u_3)_{i,j,k-\frac{1}{2}} \Phi_w(\mathbf{x}_{i,j,k-\frac{1}{2}} - \mathbf{X}_l) \left(h^{\ell_{\max}}\right)^3, \tag{3.6c}$$

in which we again consider only Cartesian grid cells on the finest level of the hierarchical grid. Analogous formulae are used to approximate Eq. (2.1f).

Eqs. (3.5a)-(3.5c) and (3.6a)-(3.6c) implicitly define discrete operators that we denote by $\boldsymbol{\mathcal{S}}[\mathbf{X}]$ and $\boldsymbol{\mathcal{S}}^*[\mathbf{X}]$, respectively. With this notation, $\mathbf{f}=\boldsymbol{\mathcal{S}}[\mathbf{X}]\mathbf{F}$, $\mathbf{n}=\boldsymbol{\mathcal{S}}[\mathbf{X}]\mathbf{N}$, $\mathbf{U}=\boldsymbol{\mathcal{S}}^*[\mathbf{X}]\mathbf{u}$, and $\mathbf{W}=\frac{1}{2}\boldsymbol{\mathcal{S}}^*[\mathbf{X}](\nabla_h\times\mathbf{u})$.

4 Temporal discretization

Unlike earlier versions of the generalized IB method [4, 5], we employ herein a second-order accurate timestepping scheme to advance $\mathbf{u}$, p, $\mathbf{X}$, and $\mathbf{D}^i$, $i=1,2,3$, over the time interval $[t^n,t^{n+1}]=[n\Delta t,(n+1)\Delta t]$. The approach that we take is similar to semi-implicit timestepping schemes used previously with the conventional IB method [10–12, 16].

We first compute initial approximations $\mathbf{X}^{n+1,*}$ and $(\mathbf{D}^i)^{n+1,*}$ to the values of $\mathbf{X}$ and $\mathbf{D}^i$, $i=1,2,3$, at time t^{n+1} via

$$\mathbf{U}^n=\boldsymbol{\mathcal{S}}^*[\mathbf{X}^n]\mathbf{u}^n, \tag{4.1a}$$

$$\mathbf{W}^n=\frac{1}{2}\boldsymbol{\mathcal{S}}^*[\mathbf{X}^n](\nabla_h\times\mathbf{u}^n), \tag{4.1b}$$

$$\frac{\mathbf{X}_l^{n+1,*}-\mathbf{X}_l^n}{\Delta t}=\mathbf{U}_l^n, \tag{4.1c}$$

$$(\mathbf{D}_l^i)^{n+1,*}=R\left(\frac{\mathbf{W}_l^n}{|\mathbf{W}_l^n|},|\mathbf{W}_l^n|\Delta t\right)(\mathbf{D}_l^i)^n, \tag{4.1d}$$

in which the matrix $R(\mathbf{e},\theta)$ is a rotation by an angle θ about the axis aligned with the unit vector $\mathbf{e}$. The rotation matrix $R(\mathbf{e},\theta)$ is defined by

$$R(\mathbf{e},\theta)=(\cos\theta)I+(1-\cos\theta)\mathbf{e}\mathbf{e}^T+(\sin\theta)(\mathbf{e}\times), \tag{4.2}$$

in which $(\mathbf{e}\times)$ is the unique antisymmetric matrix such that $(\mathbf{e}\times)\mathbf{v}=\mathbf{e}\times\mathbf{v}$ for all $\mathbf{v}$. Using the values defined at time t^n along with the predicted values defined at time t^{n+1}, we compute approximations to the current and predicted values of $\mathbf{F}$ and $\mathbf{N}$ at times t^n and t^{n+1}. These quantities are spread to the Cartesian grid via

$$\mathbf{f}^n=\boldsymbol{\mathcal{S}}[\mathbf{X}^n]\mathbf{F}^n, \tag{4.3a}$$

$$\mathbf{n}^n=\boldsymbol{\mathcal{S}}[\mathbf{X}^n]\mathbf{N}^n, \tag{4.3b}$$

$$\mathbf{f}^{n+1,*}=\boldsymbol{\mathcal{S}}\left[\mathbf{X}^{n+1,*}\right]\mathbf{F}^{n+1,*}, \tag{4.3c}$$

$$\mathbf{n}^{n+1,*}=\boldsymbol{\mathcal{S}}\left[\mathbf{X}^{n+1,*}\right]\mathbf{N}^{n+1,*}. \tag{4.3d}$$

For convenience, we define timestep-centered approximations to $\mathbf{f}$ and $\mathbf{n}$ via

$$\mathbf{f}^{n+\frac{1}{2}}=\frac{1}{2}\left(\mathbf{f}^n+\mathbf{f}^{n+1,*}\right), \tag{4.4a}$$

$$\mathbf{n}^{n+\frac{1}{2}}=\frac{1}{2}\left(\mathbf{n}^n+\mathbf{n}^{n+1,*}\right). \tag{4.4b}$$

These timestep-centered values are the discrete Eulerian force and torque densities that are applied to the fluid.

Next, we use a Runge-Kutta/Crank-Nicolson scheme to solve the incompressible Navier-Stokes equations. We first solve

$$\rho\left(\frac{\mathbf{u}^{n+1,*}-\mathbf{u}^n}{\Delta t}+\mathbf{A}^n\right)=-\nabla_h p^{n+\frac{1}{2},*}+\frac{\mu}{2}\nabla_h^2\left(\mathbf{u}^n+\mathbf{u}^{n+1,*}\right)+\mathbf{f}^{n+\frac{1}{2}}+\frac{1}{2}\nabla_h\times\mathbf{n}^{n+\frac{1}{2}}, \tag{4.5a}$$

$$\nabla_h\cdot\mathbf{u}^{n+1,*}=0, \tag{4.5b}$$

in which $\mathbf{u}^{n+1,*}$ is a discretely divergence-free intermediate approximation to $\mathbf{u}$ at time t^{n+1}, $p^{n+1/2,*}$ is an intermediate approximation to p at time t^{n+1}, and $\mathbf{A}^n\approx[\mathbf{u}^n\cdot\nabla\mathbf{u}^n]$ is computed by a staggered-grid version [36] of the xsPPM7 variant [37] of the piecewise parabolic method (PPM) [38]. We then obtain a final approximation to $\mathbf{u}$ at time t^{n+1} and to p at time $t^{n+1/2}$ by solving

$$\begin{aligned}\rho\left(\frac{\mathbf{u}^{n+1}-\mathbf{u}^n}{\Delta t}+\frac{1}{2}\left(\mathbf{A}^n+\mathbf{A}^{n+1,*}\right)\right)&\\ =-\nabla_h p^{n+\frac{1}{2}}+\frac{\mu}{2}\nabla_h^2\left(\mathbf{u}^n+\mathbf{u}^{n+1}\right)+\mathbf{f}^{n+\frac{1}{2}}+\frac{1}{2}\nabla_h\times\mathbf{n}^{n+\frac{1}{2}},&\end{aligned} \tag{4.6a}$$

$$\nabla_h\cdot\mathbf{u}^{n+1}=0, \tag{4.6b}$$

in which $\mathbf{A}^{n+1,*}\approx\left[\mathbf{u}^{n+1,*}\cdot\nabla\mathbf{u}^{n+1,*}\right]$. Notice that solving Eqs. (4.5a)-(4.5b) and Eqs. (4.6a)-(4.6b) for $(\mathbf{u}^{n+1,*},p^{n+1/2,*})$ and for $(\mathbf{u}^{n+1},p^{n+1/2})$, respectively, requires only a solver for an implicit discretization of the time-dependent incompressible Stokes equations. In our computations, we solve these systems of equations via the FGMRES algorithm [39], and we use the projection method as a preconditioner [36]. We use the most recently computed approximations to $\mathbf{u}$ and p as initial guesses for this iterative solver.

Finally, having determined $\mathbf{u}^{n+1}$ and $p^{n+1/2}$, we obtain final approximations to $\mathbf{X}$ and $\mathbf{D}^i$, $i=1,2,3$, at time t^{n+1} by computing

$$\mathbf{U}^{n+1,*}=\boldsymbol{\mathcal{S}}^*\left[\mathbf{X}^{n+1,*}\right]\mathbf{u}^{n+1}, \tag{4.7a}$$

$$\mathbf{W}^{n+1,*}=\frac{1}{2}\boldsymbol{\mathcal{S}}^*\left[\mathbf{X}^{n+1,*}\right]\left(\nabla_h\times\mathbf{u}^{n+1}\right), \tag{4.7b}$$

and by evaluating

$$\frac{\mathbf{X}_l^{n+1}-\mathbf{X}_l^n}{\Delta t}=\mathbf{U}^{n+\frac{1}{2}}, \tag{4.8a}$$

$$(\mathbf{D}_l^i)^{n+1}=R\left(\frac{\mathbf{W}_l^{n+\frac{1}{2}}}{\left|\mathbf{W}_l^{n+\frac{1}{2}}\right|},\left|\mathbf{W}_l^{n+\frac{1}{2}}\right|\Delta t\right)(\mathbf{D}_l^i)^n, \tag{4.8b}$$

in which $\mathbf{U}^{n+1/2}=\frac{1}{2}\left(\mathbf{U}^n+\mathbf{U}^{n+1,*}\right)$ and $\mathbf{W}^{n+1/2}=\frac{1}{2}\left(\mathbf{W}^n+\mathbf{W}^{n+1,*}\right)$.

5 Adaptive mesh refinement

The locally refined grid is constructed, either at the initial time or at some subsequent time, via a simple recursive procedure. First, level 0 of the grid hierarchy is defined to be a uniform-grid discretization of the physical domain U composed of one or more nonoverlapping Cartesian grid patches. Next, having generated levels $0,\cdots,\ell$, we construct level $\ell+1$ by (1) tagging cells on level ℓ for refinement, (2) covering the tagged level ℓ grid cells by rectangular boxes generated by the Berger-Rigoutsos point-clustering algorithm [40], and (3) refining the generated boxes by the integer refinement ratio $\mathfrak{n}$ to form the level $\ell+1$ grid patches. This process terminates once levels $\ell=0,\cdots,\ell_{\max}$ have each been constructed. In our scheme, cells are tagged for refinement whenever they contain one or more Lagrangian mesh nodes. A tag buffer ensures that cells within the support of $\Phi_w(\mathbf{x}-\mathbf{X}_l)$ for each Lagrangian mesh node l are also tagged for refinement. These tagging criteria ensure that the immersed structure is embedded within the finest level of the Cartesian grid hierarchy and, moreover, that the support of $\Phi_w(\mathbf{x}-\mathbf{X}_l)$ is contained within the finest level of the grid for each Lagrangian node l. This latter property allows us to use the simple discretization of the Lagrangian-Eulerian interaction equations described in Section 3.3.

The locally refined grid is regenerated at a fixed interval that is determined by the composite-grid CFL condition,

$$\Delta t \leq C \min_{0\leq\ell\leq\ell_{\max}} \frac{h^\ell}{\|\mathbf{u}(\mathbf{x}_{i,j,k})\|_\infty}, \tag{5.1}$$

in which C is the CFL number. With the present scheme, a necessary condition for stability is $C \leq \frac{1}{2}$. We regenerate the Cartesian grid hierarchy every $\lfloor 1/C \rfloor \geq 2$ timesteps. Doing so ensures that the immersed structure cannot escape from the finest level of the grid hierarchy.

When we regenerate the Cartesian grid hierarchy, we must transfer the values of $\mathbf{u}$ and p from the old locally refined grid to the new one. In newly refined regions of U, we use a recursive version of the divergence- and curl-preserving interpolation scheme of Tóth and Roe [41] to define $\mathbf{u}$, and we use trilinear interpolation to define p. In newly coarsened regions of U, we define $\mathbf{u}$ and p to be the averages of the overlying fine-grid values of the old grid hierarchy. This procedure ensures that $\mathbf{u}$ remains discretely divergence free. In particular, it is not necessary to project the interpolated velocity field to enforce the discrete incompressibility condition.

6 Implementation

This adaptive version of the generalized IB method is implemented in the IBAMR software framework [42], an open-source library for developing fluid-structure interaction

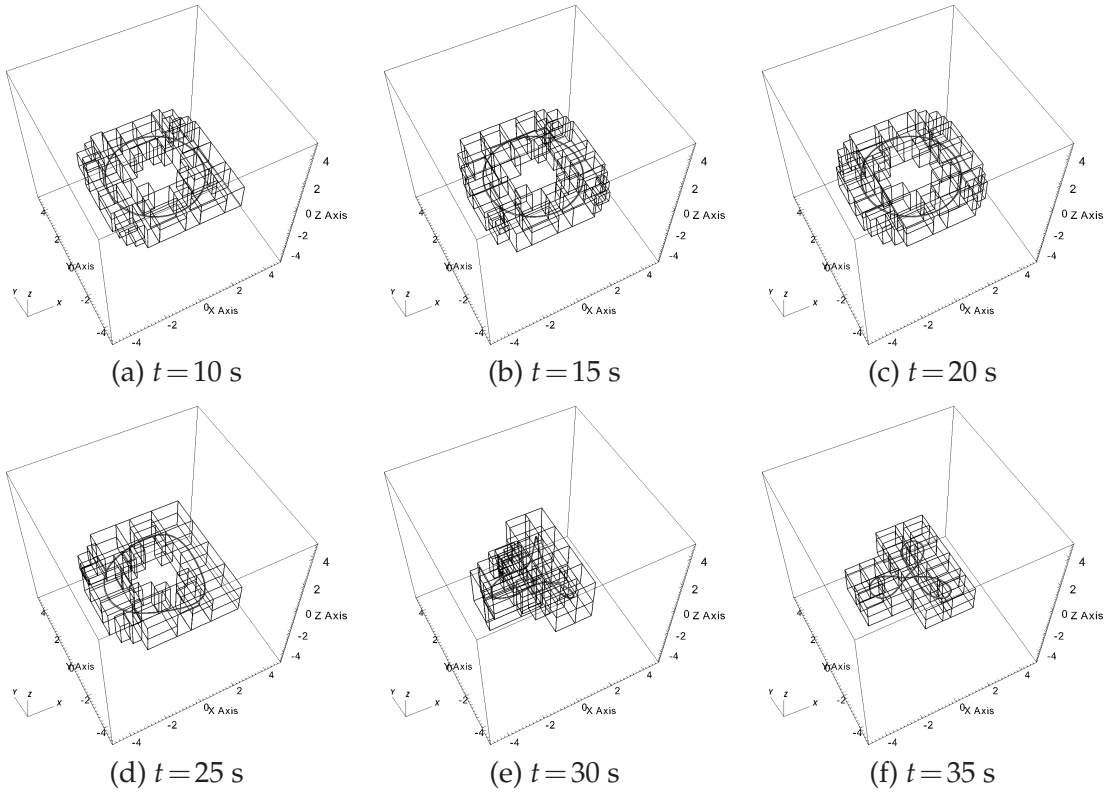

(a) $t=10$ s (b) $t=15$ s (c) $t=20$ s

(d) $t=25$ s (e) $t=30$ s (f) $t=35$ s

Figure 4: Time course for a three-level adaptive simulation with $N^{\ell_{\max}}=256$ and refinement ratio $\mathrm{n}=4$ between levels. The immersed elastic ring is shown in silver. For clarity, only the grid patches that comprise the finest level of the grid hierarchy are shown. Notice that high spatial resolution is deployed only in the vicinity of the immersed elastic ring.

models that use the IB method. The IBAMR framework uses SAMRAI [43–45] to manage the locally refined Cartesian grid, and it uses PETSc [46–48] to manage the immersed Lagrangian mesh and to provide iterative solvers such as FGMRES. IBAMR provides custom implementations of multilevel multigrid preconditioners that are based on the FAC algorithm [49–51]. Uniform-grid geometric multigrid solvers from the *hypre* library [52, 53] are used by IBAMR as coarse-grid solvers in its cell- and face-centered implementations of the FAC algorithm. In this work, these multilevel preconditioners are used as subdomain solvers in the projection method-based preconditioner for the time-dependent incompressible Stokes equations [36].

7 Empirical convergence study

We first perform an empirical convergence study to demonstrate the convergence properties of our adaptive discretization. These simulations were performed on the `cardiac` cluster at New York University, which is comprised of 80 Sun Microsystems, Inc., Sun

Table 1: Numerical and physical parameters for the simulations of Section 7.

parameter	symbol	value
length of computational domain U	L	10 cm
number of grid levels	$\ell_{\max}+1$	2
refinement ratio between levels	$\mathfrak{n}$	4
effective number of cells on level $\ell_{\max}$	$N^{\ell_{\max}}$	64, 128, 256, 512
effective fine-grid spacing	$h^{\ell_{\max}}$	1.5625, 0.78125, 0.390625, 0.1953125 mm
radius of unstressed ring	r_0	2.5 cm
timestep size	Δt	0.02, 0.01, 0.005, 0.0025 s
fluid density	ρ	1.0 g/cm^3
fluid viscosity	μ	0.01 g/(cm·s)
bending modulus	$a=a_1=a_2$	0.3 g·cm^3/s^2
twist modulus	a_3	0.3 g·cm^3/s^2
shear modulus	$b=b_1=b_2$	54 g·cm/s^2
stretch modulus	b_3	36 g·cm/s^2

Blade X8440 server modules interconnected by an InfiniBand network. Each compute server is equipped with four 2.3 GHz quad-core AMD Barcelona 8356 processors with 2 GB memory per core. Simulations were run in parallel using as many as six quad-processor quad-core nodes, for a total of 96 cores per job.

Using the physical and numerical parameters shown in Table 1, we consider a twisted elastic ring with $q=5$, $\epsilon=0.01$, and $\kappa=\tau=0$. We consider $N=N^{\ell_{\max}}=64$, 128, 256, and 512, and we set $w=1.5625$ mm, so that the kernel function $\Phi_w(\mathbf{x})$ is supported on at least a $4\times4\times4$ box of Cartesian grid cells in each case that we consider. The elastic ring is rediscretized for each value of $N^{\ell_{\max}}$ so that $\Delta s\approx\frac{1}{2}h^{\ell_{\max}}$. For the purposes of this convergence study, we also apply a small additional Eulerian background force to the fluid,

$$\mathbf{f}_{\mathrm{b}}(\mathbf{x},t)=(0,0,10\sin(2\pi x_1/L)\sin(2\pi x_2/L)\exp(-10t)t). \tag{7.1}$$

This additional background force ensures that the final orientation of the ring is consistent for all grid spacings. The dynamics of the ring are shown in Fig. 5. We estimate the

(a) $t=5$ s (b) $t=10$ s (c) $t=15$ s (d) $t=20$ s (e) $t=30$ s

Figure 5: Time course of ring configurations from the convergence study of Section 7. The ring has essentially reached its final equilibrium configuration by time $t=30$ s.

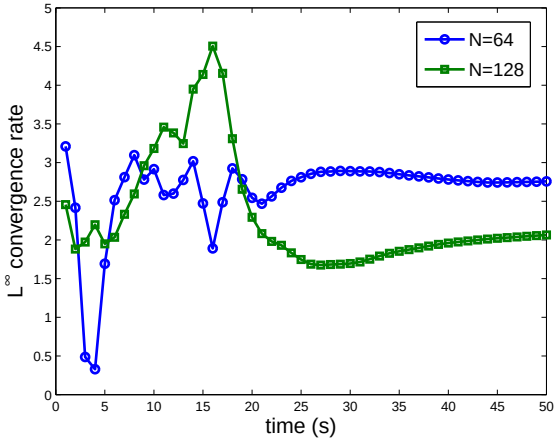

Figure 6: Empirical L^∞ convergence rates as functions of time for $N = N^{\ell_{\max}} = 64$ and 128. The empirical convergence rate is defined by $\log_2 \left(\left\| \mathbf{X}^N - \mathbf{X}^{2N} \right\|_\infty / \left\| \mathbf{X}^{2N} - \mathbf{X}^{4N} \right\|_\infty \right)$.

convergence rate of the method for $N = N^{\ell_{\max}}$ in a standard way by computing

$$\log_2 \left(\frac{\left\| \mathbf{X}^N - \mathbf{X}^{2N} \right\|_\infty}{\left\| \mathbf{X}^{2N} - \mathbf{X}^{4N} \right\|_\infty} \right), \tag{7.2}$$

in which here, $\mathbf{X}^N$ denotes the solution obtained on a locally refined Cartesian grid with $N = N^{\ell_{\max}}$. Results for $N = N^{\ell_{\max}} = 64$ and 128 are summarized in Fig. 6. These data suggest that the position of the ring is converging at an essentially second-order rate for the present problem, although these data also suggest that the scheme may not have yet reached its asymptotic rate of convergence. Despite the fact that we use a locally-refined Eulerian discretization that suffers from a localized reduction in accuracy at coarse-fine interfaces, these convergence results also suggest that this reduction in accuracy is unlikely to dominate the error in the method at grid spacings that are currently practical for three-dimensional simulations.

8 Dynamic stability analysis

With the physical and numerical parameters shown in Table 2, we use the adaptive generalized IB method to study the stability of various conformations of the elastic ring. Most of these simulations were performed on the `cardiac` cluster at New York University that was described previously in Section 7. Simulations that were run in parallel used two quad-processor quad-core nodes, for a total of 24 cores. Except where otherwise noted, throughout this section, $w = 2h^{\ell_{\max}}$, so that the width of the support of Φ_w is $8h^{\ell_{\max}} = 6.25$ mm. In most cases, the peak CFL number in a particular simulation is less than approximately 0.3, although in some cases the peak CFL number may be as high as

Table 2: Numerical and physical parameters for the simulations of Section 8.

parameter	symbol	value
length of computational domain U	L	10 cm
number of grid levels	$\ell_{\max}+1$	3
refinement ratio between levels	$\mathfrak{n}$	4
effective number of cells on level $\ell_{\max}$	$N^{\ell_{\max}}$	128
effective fine-grid spacing	$h^{\ell_{\max}}$	0.78125 mm
radius of unstressed ring	r_0	2.5 cm
timestep size	Δt	0.01 s
fluid density	ρ	1.0 g/cm^3
fluid viscosity	μ	0.01 g/(cm·s)
bending modulus	$a=a_1=a_2$	0.3 g·cm^3/s^2
twist modulus	a_3	0.1–0.6 g·cm^3/s^2
shear modulus	$b=b_1=b_2$	54 g·cm/s^2
stretch modulus	b_3	54 g·cm/s^2

approximately 0.45. In general, higher twist densities result in larger flow velocities and larger peak CFL numbers. We remark, however, that the rod and the surrounding fluid are nearly quiescent for the significant portion of the simulation that occurs prior to the onset of the instability.

We first verified that corresponding values of the twist density τ (with q set to zero) and the twist number q (with τ set to zero) yield the same equilibrium configurations for $\tau=0.4,0.8,\cdots,2$. Note that these values of τ correspond to $q=1,2,\cdots,5$. These stable equilibria are shown as a function of τ in Fig. 7. The corresponding configurations obtained by varying q are the same as those of Fig. 7 and therefore are not shown. For simplicity, for the remainder of this work, we set $q=0$ and use τ to control the intrinsic twist of the ring.

Fig. 7 shows representative stable equilibrium configurations for various intrinsic twist densities and for two different choices of the ratio of twisting modulus to bending modulus, a_3/a. In these simulations, the ring is intrinsically straight, i.e., $\kappa=0$. For small values of the twist density, the twisted ring remains stable, but for sufficiently large twist values, the ring becomes unstable, undergoes a writhing instability, and eventually reaches a stable coiled configuration. In this process, the torsional energy related to the twist of the elastic ring is converted into bending energy by the change in the shape of the ring. We remark that the limiting configurations shown in Fig. 7 are the same as those achieved in previous simulations using a uniform-grid version of the generalized IB method [4].

According to Michell [22] and Goriely et al. [21, 54], the critical value of twist that separates stable and unstable configurations of an intrinsically straight ring is given by

$$\tau_c=\sqrt{3}\frac{a}{a_3 r_0}. \tag{8.1}$$

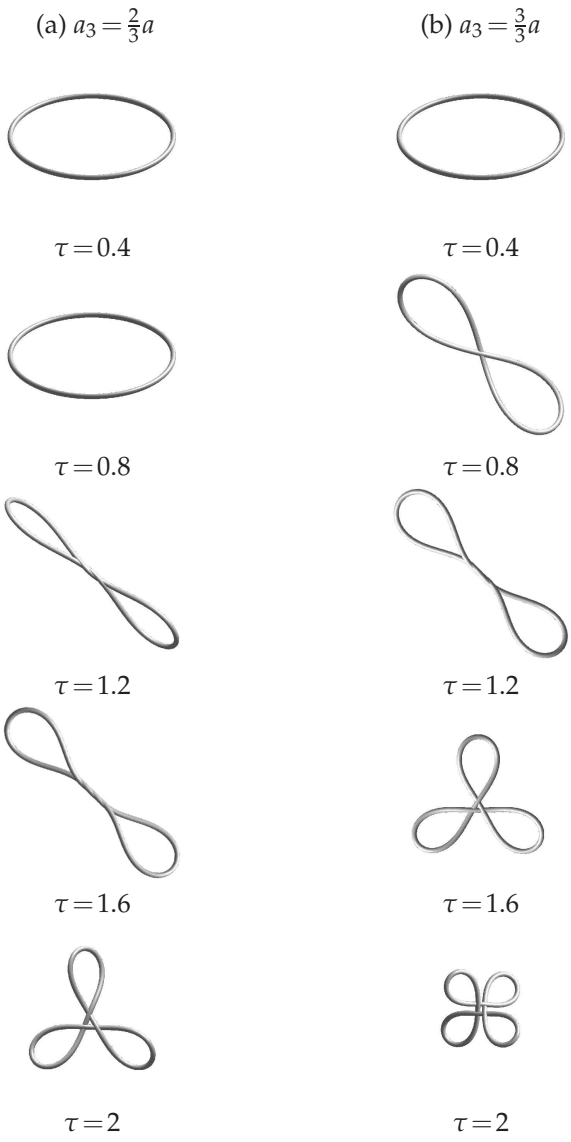

Figure 7: A collection of representative stable equilibria in which a_3/a, the ratio of twisting to bending modulus, is $2/3$ or $3/3$ for various values of the intrinsic twist density τ. Recall that the total number of twists in the ring is 2.5τ. The bending modulus is set to $a=0.3$. The ring here is intrinsically straight, i.e., $\kappa=0$.

Defining the total twist angle in the ring by

$$T_{\mathrm{w}}=2\pi r_0\tau, \tag{8.2}$$

the critical total twist angle is

$$T_{\mathrm{w}}^{\mathrm{c}}=2\pi\sqrt{3}\frac{a}{a_3}. \tag{8.3}$$

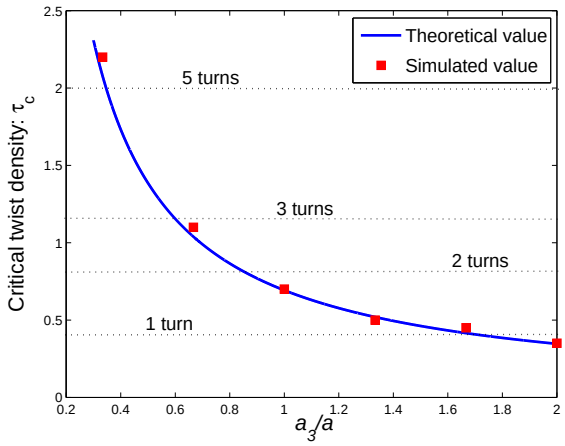

Figure 8: Comparison of the critical value of the twist density obtained from computational experiments with theoretical values from elastic rod theory depending on the ratio of twisting to bending modulus. The number of full turns is indicated for each value of the twist density.

Thus, the twisted ring becomes unstable for $T_w > T_w^c$, independent of the radius of the ring. In other words, for a fixed ratio of torsional to flexural rigidity, the number of turns in the ring will determine the instability threshold of the elastic ring. With $a_3/a = 2/3$, the critical twist density τ_c is

$$\tau_c = \sqrt{3}\frac{0.3}{0.2\times 2.5} \approx 1.0392. \tag{8.4}$$

Thus, the critical twist number q_c is given by

$$q_c = \frac{c\tau_c}{2\pi} \approx 2.5981, \tag{8.5}$$

in which $c = 2\pi r_0$ is the circumference of the unstressed ring. Eq. (8.5) implies that if there are more than two full turns along the ring, then the twisted ring becomes unstable, as can be seen in Fig. 7. Our simulations confirm that the critical twist density decreases as the ratio of twisting to bending modulus increases. Fig. 8 compares the theoretical values of the critical twist with values obtained from our simulations. For a fixed bending modulus, the critical value of torsion is inversely proportional to the twisting modulus. Simulation data shown in Fig. 8 fit well with the theoretical values. We remark that if the twist density is a sufficient amount larger than the instability threshold, and if the twist modulus is at least somewhat larger than the bending modulus, then the final configuration becomes very sensitive to perturbations.

We also investigate whether changing the effective thickness of the rod has any effect on the equilibrium configuration of the intrinsically straight elastic ring. We do so by choosing different values for the parameter w that controls the breadth of the kernel function $\Phi_w(\mathbf{x})$. Specifically, we choose $w = h^{\ell_{\max}}$, $2h^{\ell_{\max}}$, and $4h^{\ell_{\max}}$, so that $\Phi_w(\mathbf{x})$ is supported on a $4\times4\times4$, $8\times8\times8$, or $16\times16\times16$ box of Cartesian grid cells on level $\ell_{\max}$. We find that,

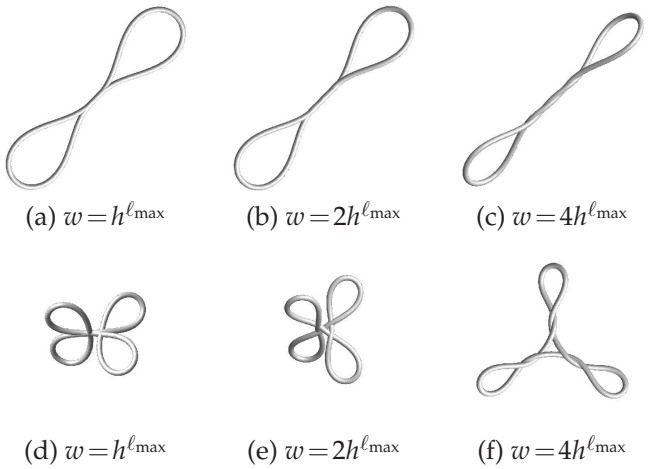

(a) $w=h^{\ell\max}$ (b) $w=2h^{\ell\max}$ (c) $w=4h^{\ell\max}$

(d) $w=h^{\ell\max}$ (e) $w=2h^{\ell\max}$ (f) $w=4h^{\ell\max}$

Figure 9: Equilibrium configuration as a function of effective rod thickness w. The top row corresponds to $\tau=1.6$, and the bottom row corresponds to $\tau=2.8$. In these simulations, $\kappa=0$, $a=0.3$, and $a_3=0.2$.

at lower twist densities, variations in the effective thickness of the rod do not appear to affect the equilibrium configuration of the elastic ring. Moreover, at least for the effective thicknesses considered herein, the value of the critical twist density τ_c is insensitive to the value of w, and the results for $w=h^{\ell\max}$ and $w=4h^{\ell\max}$ are the same as those shown in Fig. 8 for $w=2h^{\ell\max}$. At higher twist densities, however, the dynamics and equilibria of the unstable ring vary with w. Representative results are shown in Fig. 9.

We next consider an elastic ring that is intrinsically curved, with the curvature uniformly distributed along the rod. Fig. 10 shows the limiting configurations in which

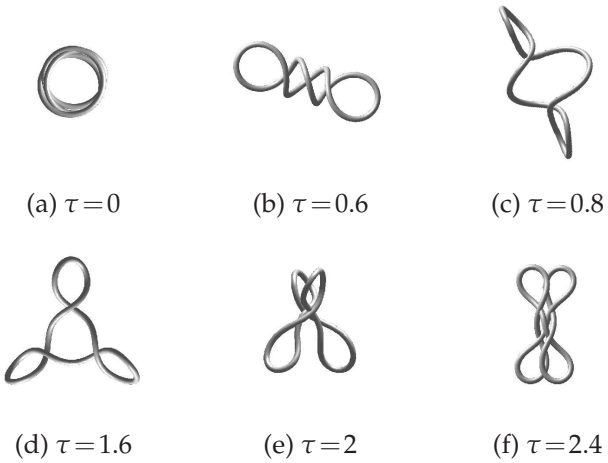

(a) $\tau=0$ (b) $\tau=0.6$ (c) $\tau=0.8$

(d) $\tau=1.6$ (e) $\tau=2$ (f) $\tau=2.4$

Figure 10: Equilibrium configurations of the intrinsically curved ring as a function of the twist density τ. In these simulations, $\kappa=\kappa_1=1.2$, $\kappa_2=0$, $a=0.3$, and $a_3=0.2$. See Fig. 11 for the time evolution of case (a), for which the equilibrium configuration is a 3-covered ring.

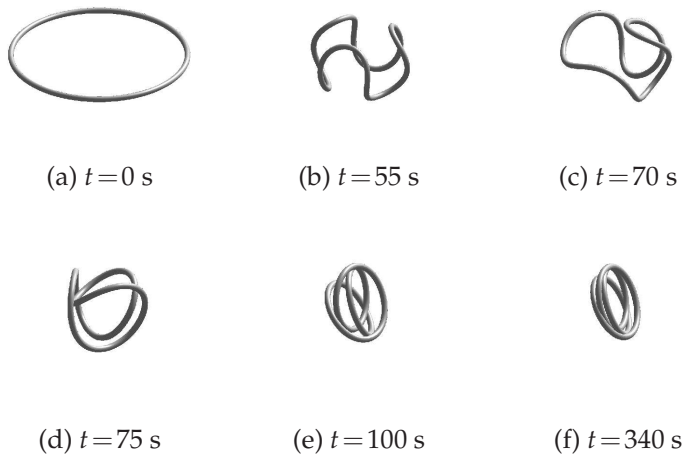

(a) $t=0$ s (b) $t=55$ s (c) $t=70$ s

(d) $t=75$ s (e) $t=100$ s (f) $t=340$ s

Figure 11: Dynamical motion of an intrinsically curved ring at various times. In this simulation, $\kappa=\kappa_1=1.2$, $\kappa_2=0$, $\tau=0$, $a=0.3$, and $a_3=0.2$. Notice that the ring shown in this figure is not twisted.

the intrinsic curvature is set to $\kappa=1.2$ for various values of the twist density, and with the bending and twisting moduli respectively set to $a=0.3$ and $a_3=0.2$. It is clear that the equilibrium configurations are quite different from those of the intrinsically straight ring; compare to Fig. 7(a). In general, for a sufficiently small value of τ with constant nonzero intrinsic curvature, the stable equilibrium configuration of the ring is that of an m-covered ring satisfying the relation

$$m=\frac{c\kappa}{2\pi}, \tag{8.6}$$

in which c is the circumference of the unstressed ring. For instance, with $\kappa=1.2$, an initially 1-covered ring deforms into a 3-covered ring, as shown in Fig. 10(a). See also Fig. 11 for the transient shapes of the 3-covered ring at different times. For larger $\tau>0$ with nonzero κ, the ring becomes intrinsically helical and buckles as τ increases. This phenomenon is similar to that of intrinsically curved open rods: for sufficiently small values of τ, the open rod takes the form of a stable helix; however, as τ increases, the helical radius tends to zero, and the rod buckles [5,54,55]. Fig. 10(b) and (d) show cases in which local helical regions develop along the ring. As τ increases, the helical radius decreases and ultimately yields a degenerate helical configuration in which the ring is locally straight.

The equilibrium configurations of rings that have only localized regions of nonzero intrinsic curvature are also quite different from those of intrinsically straight rings, and from those that possess uniformly distributed nonzero intrinsic curvature. Fig. 12 illustrates five cases of rings with different numbers of locally curved regions. The intrinsic curvature of each locally curved section is set to $\kappa=1.2$, and the remainder of the rod is straight, i.e., $\kappa=0$. The intrinsic twist is uniformly distributed along the rod as $\tau=1.6$.

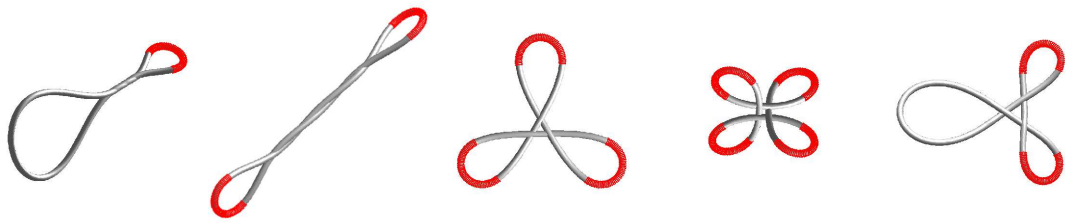

Figure 12: Equilibrium configurations of rings that contain only localized sections of nonzero intrinsic curvature. The curved sections of each rod are shown in red. In the curved sections, $\kappa=1.2$, whereas $\kappa=0$ in the remainder of the ring. In these simulations, $\tau=1.6$, $a=0.3$, and $a_3=0.2$.

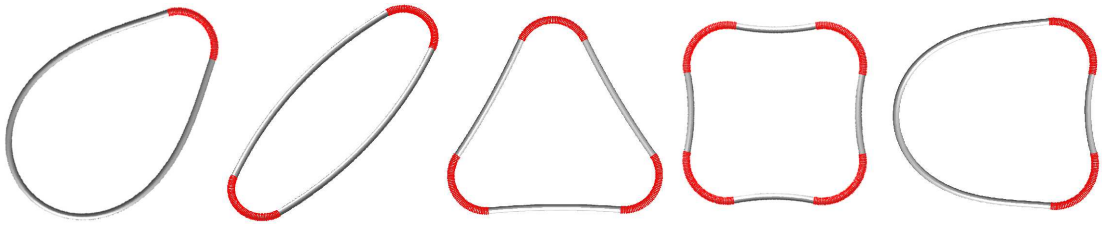

Figure 13: Equilibrium configurations of rings without self-contact. Each ring contains only localized sections of nonzero intrinsic curvature. The curved sections of each rod are shown in red. In the curved sections, $\kappa=1.2$, whereas $\kappa=0$ in the remainder of the ring. In these simulations, $\tau=0$, $a=0.3$, and $a_3=0.2$.

Here, the bending and twisting moduli are set to $a=0.3$ and $a_3=0.2$, respectively. For comparison, see Fig. 7(a) with $\tau=1.6$ and Fig. 10(d). Our simulations show that intrinsically curved sections of the ring localize to the ends of loops placed under high bending energy. Such loop localization has been experimentally observed in plasmid DNA [23,28]. We expect that a sufficiently long ring with locally curved sections would evolve into a branched form, with each branch taking the plectonemic form. We remark that, for the intrinsically straight ring, it is known that the circle is the only stable configuration without self-contact [54,56], and it is expected that there are no stable configurations without self-contact of an intrinsically curved ring with uniform intrinsic curvature [23]. However, a ring with only *localized* regions of nonzero intrinsic curvature has stable noncircular configurations without self-contact, as can be clearly seen in Fig. 13.

9 Conclusions and future directions

In this paper, we have presented an adaptive, formally second-order accurate generalized IB method that describes the dynamics of an elastic rod immersed in fluid. The method uses a version of Kirchhoff rod theory that describes the elasticity of the rod in terms of the position of its center line together with a Lagrangian field of director vectors attached to that center line. We have empirically demonstrated that this method yields essentially second-order convergence rates, and we have analyzed the instability of an elastic ring immersed in fluid.

It is well known that the intrinsic curvature and twist of an elastic ring play important roles in determining its equilibrium configuration, as also demonstrated by our simulations. In this work, we considered three cases: (1) rings that are intrinsically straight; (2) rings that are intrinsically curved; and (3) rings that have only local regions of nonzero intrinsic curvature. In cases in which the ring is intrinsically straight but twisted, we found that the ring remains stable for low twist values but that it becomes unstable for larger twist values, and we determined the critical twist values that separate stable configurations from unstable ones. These empirically determined critical twist values correspond closely to theoretical values obtained from either a linearized static analysis or a perturbation analysis of an elastic ring. In cases in which the ring is intrinsically curved with uniform nonzero curvature and nonzero twist, we found that the ring tends to take the form of a closed helical rod. As the intrinsic twist increases, the ring deforms into a folding structure with multiple self-contacts. For intrinsically curved rings with no intrinsic twist, the ring deforms to a multicovered ring of a smaller radius. In cases in which the ring has only localized regions of nonzero intrinsic curvature, we observed noncircular stable solutions without self-contact. In these cases, the shape of the stable solution depends on both the position and also the number of such locally curved sections. These equilibrium shapes are likely also to depend on material and geometrical properties, but we have not investigated this possibility in this work. We remark that cases involving spatial inhomogeneities in intrinsic curvature or twist are especially relevant to many potential applications of this simulation methodology.

We expect that the adaptive version of the generalized IB method will find numerous applications, especially in biological fluid dynamics, for problems in which thin, filamentous structures interact with a viscous fluid. One example is the supercoiling dynamics of ranges of DNA sequences that are fully or partially curved, for which the intrinsic curvature of the DNA would determine its configuration at equilibrium. Another interesting potential application of this method is to simulate the fluid mechanics of swimming bacteria with helical flagella. Simulating flagellar motion requires the use of high spatial resolution, so as to resolve the flow in the neighborhood of the flagellum. Because the aspect ratio of the flagellum is approximately 250, with the length of the flagellum being approximately 5 μm and the thickness of being only approximately 20 nm [57], it may be crucial to deploy an adaptive discretization approach to obtain resolved numerical simulations. The present adaptive method therefore promises to enable us to investigate the detailed dynamics of bacteria with unprecedented fidelity.

Acknowledgments

B.E.G. gratefully acknowledges research support from American Heart Association award 10SDG4320049 and National Science Foundation awards DMS 1016554 and OCI 1047734. S.L. gratefully acknowledges research support from National Science Foundation award DMS 0815751. Most computations were performed at New York University using computer facilities funded in large part by a generous donation by St. Jude Medical, Inc.

References

[1] C. S. Peskin. Flow patterns around heart valves: A digital computer method for solving the equations of motion. PhD thesis, Albert Einstein College of Medicine, 1972.

[2] C. S. Peskin. Numerical analysis of blood flow in the heart. J. Comput. Phys., 25(3):220–252, 1977.

[3] C. S. Peskin. The immersed boundary method. Acta Numer., 11:479–517, 2002.

[4] S. Lim, A. Ferent, X. S. Wang, and C. S. Peskin. Dynamics of a closed rod with twist and bend in fluid. SIAM J. Sci. Comput., 31(1):273–302, 2008.

[5] S. Lim. Dynamics of an open elastic rod with intrinsic curvature and twist in a viscous fluid. Phys. Fluid, 22(2):024104, 2010.

[6] C.-L. Lu and N. C. Perkins. Nonlinear spatial equilibria and stability of cables under uniaxial torque and thrust. J. Appl. Mech., 61(4):879–886, 1994.

[7] S. Goyal, N. C. Perkins, and C. L. Lee. Nonlinear dynamics and loop formation in Kirchhoff rods with implications to the mechanics of DNA and cables. J. Comput. Phys., 209(1):371–389, 2005.

[8] S. Goyal, T. Lillian, S. Blumberg, J.-C. Meiners, E. Meyhöfer, and N. C. Perkins. Intrinsic curvature of DNA influences LacR-mediated looping. Biophys. J., 93(12):4342–4359, 2007.

[9] A. M. Roma, C. S. Peskin, and M. J. Berger. An adaptive version of the immersed boundary method. J. Comput. Phys., 153(2):509–534, 1999.

[10] B. E. Griffith, R. D. Hornung, D. M. McQueen, and C. S. Peskin. An adaptive, formally second order accurate version of the immersed boundary method. J. Comput. Phys., 223(1):10–49, 2007.

[11] B. E. Griffith, R. D. Hornung, D. M. McQueen, and C. S. Peskin. Parallel and adaptive simulation of cardiac fluid dynamics. In M. Parashar and X. Li, editors, Advanced Computational Infrastructures for Parallel and Distributed Adaptive Applications. John Wiley and Sons, Hoboken, NJ, USA, 2009.

[12] B. E. Griffith, X. Luo, D. M. McQueen, and C. S. Peskin. Simulating the fluid dynamics of natural and prosthetic heart valves using the immersed boundary method. Int. J. Appl. Mech., 1(1):137–177, 2009.

[13] B. E. Griffith. Immersed boundary model of aortic heart valve dynamics with physiological driving and loading conditions. Int. J. Numer. Meth. Biomed. Eng. To appear.

[14] F. H. Harlow and J. E. Welch. Numerical calculation of time-dependent viscous incompresible flow of fluid with free surface. Phys. Fluid, 8(12):2182–2189, 1965.

[15] B. E. Griffith. On the volume conservation of the immersed boundary method. Commun. Comput. Phys. In press.

[16] B. E. Griffith and C. S. Peskin. On the order of accuracy of the immersed boundary method: Higher order convergence rates for sufficiently smooth problems. J. Comput. Phys., 208(1):75–105, 2005.

[17] D. Boffi, L. Gastaldi, L. Heltai, and C. S. Peskin. On the hyper-elastic formulation of the immersed boundary method. Comput. Meth. Appl. Mech. Engrg., 197(25–28):2210–2231, 2008.

[18] B. D. Coleman and D. Swigon. Theory of supercoiled elastic rings with self contact and its application to DNA plasmids. J. Elasticity, 60(3):171–221, 2000.

[19] B. D. Coleman, D. Swigon, and I. Tobias. Elastic stability of DNA configurations: II. Supercoiled plasmids with self contact. Phys. Rev. E, 61(1):759–770, 2000.

[20] Y. Y. Biton, B. D. Coleman, and D. Swigon. On bifurcations of equilibria of intrinsically

curved, electrically charged, rod-like structures that model DNA molecules in solution. J. Elasticity, 87(2–3):187–210, 2007.
[21] A. Goriely. Twisted elastic rings and the rediscoveries of Michell's instability. J. Elasticity, 84(3):281–299, 2006.
[22] J. H. Michell. On the stability of a bent and twisted wire. Messeng. Math., 19:181–184, 1890.
[23] I. Tobias and W. K. Olson. The effect of intrinsic curvature on supercoiling: predictions of elasticity theory. Biopolymers, 33(4):639–646, 1993.
[24] I. Tobias, B. D. Coleman, and M. Lembo. A class of exact dynamical solutions in the elastic rod model of DNA with implications for the theory of fluctuations in the torsional motion of plasmids. J. Chem. Phys., 105(6):2517–2526, 1996.
[25] H. Qian and J. H. White. Terminal twist induced continuous writhe of a circular rod with intrinsic curvature. J. Biomol. Struct. Dyn., 16(3):663–669, 1998.
[26] Z. Haijun and O.-Y. Zhong-can. Spontaneous curvature-induced dynamical instability of Kirchhoff filaments: application to DNA kink deformations. J. Chem. Phys., 110(2):1247–1251, 1999.
[27] R. S. Manning and K. A. Hoffman. Stability of n-covered circles for elastic rods with constant planar intrinsic curvature. J. Elasticity, 62(1):1–23, 2001.
[28] C. H. Laundon and J. D. Griffith. Curved helix segments can uniquely orient the topology of supertwisted DNA. Cell, 52(4):545–549, 1988.
[29] W. R. Bauer, R. A. Lund, and J. H. White. Twist and writhe of a DNA loop containing intrinsic bends. Proc. Natl. Acad. Sci. USA, 90(3):833–837, 1993.
[30] T. T. Bringley and C. S. Peskin. Validation of a simple method for representing spheres and slender bodies in an immersed boundary method for Stokes flow on an unbounded domain. J. Comput. Phys., 227(11):5397–5425, 2008.
[31] S. S. Antman. Nonlinear Problems of Elasticity. Springer-Verlag, 1995.
[32] M. J. Berger and P. Colella. Local adaptive mesh refinement for shock hydrodynamics. J. Comput. Phys., 82(1):64–84, 1989.
[33] M. L. Minion. A projection method for locally refined grids. J. Comput. Phys., 127(1):158–178, 1996.
[34] D. F. Martin and P. Colella. A cell-centered adaptive projection method for the incompressible Euler equations. J. Comput. Phys., 163(2):271–312, 2000.
[35] D. F. Martin, P. Colella, and D. Graves. A cell-centered adaptive projection method for the incompressible Navier-Stokes equations in three dimensions. J. Comput. Phys., 227(3):1863–1886, 2008.
[36] B. E. Griffith. An accurate and efficient method for the incompressible Navier-Stokes equations using the projection method as a preconditioner. J. Comput. Phys., 228(20):7565–7595, 2009.
[37] W. J. Rider, J. A. Greenough, and J. R. Kamm. Accurate monotonicity- and extrema-preserving methods through adaptive nonlinear hybridizations. J. Comput. Phys., 225(2):1827–1848, 2007.
[38] P. Colella and P. R. Woodward. The piecewise parabolic method (PPM) for gas-dynamical simulations. J. Comput. Phys., 54(1):174–201, 1984.
[39] Y. Saad. A flexible inner-outer preconditioned GMRES algorithm. SIAM J. Sci. Comput., 14(2):461–469, 1993.
[40] M. J. Berger and I. Rigoutsos. An algorithm for point clustering and grid generation. IEEE Trans. Syst. Man. Cybern., 21(5):1278–1286, 1991.
[41] G. Tóth and P. L. Roe. Divergence- and curl-preserving prolongation and restriction formu-

las. J. Comput. Phys., 180(2):736–750, 2002.
[42] IBAMR: An adaptive and distributed-memory parallel implementation of the immersed boundary method. `http://ibamr.googlecode.com`.
[43] SAMRAI: Structured Adaptive Mesh Refinement Application Infrastructure. `http://www.llnl.gov/CASC/SAMRAI`.
[44] R. D. Hornung and S. R. Kohn. Managing application complexity in the SAMRAI object-oriented framework. Concurrency Comput. Pract. Ex., 14(5):347–368, 2002.
[45] R. D. Hornung, A. M. Wissink, and S. R. Kohn. Managing complex data and geometry in parallel structured AMR applications. Eng. Comput., 22(3–4):181–195, 2006.
[46] S. Balay, K. Buschelman, W. D. Gropp, D. Kaushik, M. G. Knepley, L. C. McInnes, B. F. Smith, and H. Zhang. PETSc Web page, 2009. `http://www.mcs.anl.gov/petsc`.
[47] S. Balay, K. Buschelman, V. Eijkhout, W. D. Gropp, D. Kaushik, M. G. Knepley, L. C. McInnes, B. F. Smith, and H. Zhang. PETSc users manual. Technical Report ANL-95/11 - Revision 3.0.0, Argonne National Laboratory, 2008.
[48] S. Balay, V. Eijkhout, W. D. Gropp, L. C. McInnes, and B. F. Smith. Efficient management of parallelism in object oriented numerical software libraries. In E. Arge, A. M. Bruaset, and H. P. Langtangen, editors, Modern Software Tools in Scientific Computing, pages 163–202. Birkhäuser Press, 1997.
[49] S. F. McCormick. Multilevel Adaptive Methods for Partial Differential Equations. Society for Industrial and Applied Mathematics, Philadelphia, PA, USA, 1989.
[50] S. F. McCormick, S. M. McKay, and J. W. Thomas. Computational complexity of the fast adaptive composite grid (FAC) method. Applied Numerical Mathematics, 6(3):315–327, 1989.
[51] S. F. McCormick. Multilevel Projection Methods for Partial Differential Equations. Society for Industrial and Applied Mathematics, Philadelphia, PA, USA, 1992.
[52] *hypre*: High performance preconditioners. `http://www.llnl.gov/CASC/hypre`.
[53] R. D. Falgout and U. M. Yang. *hypre*: a library of high performance preconditioners. In P. M. A. Sloot, C. J. K. Tan, J. J. Dongarra, and A. G. Hoekstra, editors, Computational Science - ICCS 2002 Part III, volume 2331 of Lecture Notes in Computer Science, pages 632–641. Springer-Verlag, 2002. Also available as LLNL Technical Report UCRL-JC-146175.
[54] A. Goriely and M. Tabor. The nonlinear dynamics of filaments. Nonlinear Dynam., 21(1):101–133, 2000.
[55] N. Chouaieb, A. Goriely, and J. H. Maddocks. Helices. Proc. Natl. Acad. Sci. USA, 103(25):9398–9403, 2006.
[56] M. Le Bret. Twist and writhing in short circular DNAs according to first-order elasticity. Biopolymers, 23(10):1835–1867, 1984.
[57] R. M. Macnab. Flagella and motility. In F. C. Neidhardt, R. Curtiss III, J. L. Ingraham, E. C. C. Lin, K. B. Low, B. Magasanik, W. S. Reznikoff, M. Riley, M. Schaechter, and H. E. Umbarger, editors, Escherichia coli and Salmonella: Cellular and Molecular Biology, pages 123–145. American Society for Microbiology, Washington, DC, second edition, 1996.